

Cite this: *J. Mater. Chem.*, 2012, **22**, 11396

www.rsc.org/materials

PAPER

## Transition metal-doped rare earth vanadates: a regenerable catalytic material for SOFC anodes

Lawrence Adijanto, Venu Balaji Padmanabhan, Rainer Küngas, Raymond J. Gorte and John M. Vohs\*

Received 21st March 2012, Accepted 26th April 2012

DOI: 10.1039/c2jm31774e

The physical and electrochemical properties of cerium vanadates in which a portion of the cerium cations have been substituted with transition metals ( $\text{Ce}_{1-x}\text{TM}_x\text{VO}_{4-0.5x}$ , TM = Ni, Co, Cu) were investigated and their suitability for use in solid oxide fuel cell (SOFC) anodes was assessed. Similar to other transition metal doped perovskites, the metals were found to move out of and into the oxide lattice in response to exposure to reducing and oxidizing conditions at elevated temperatures. This process produces nanoparticle metal catalysts that decorate the surface of the conductive cerium vanadate. Solid oxide fuel cells (SOFC) with  $\text{Ce}_{1-x}\text{TM}_x\text{VO}_3$ -YSZ composite anodes exhibited high electrochemical activity. It was also demonstrated that doping with the alkaline earth ions,  $\text{Ca}^{2+}$  and  $\text{Sr}^{2+}$  enhances the electronic conductivity of the vanadate and  $\text{Ce}_{0.7}\text{Sr}_{0.1}\text{Ni}_{0.2}\text{VO}_3$ -YSZ composite SOFC anodes were found to have both high electrochemical activity and unusually high redox stability.

## Introduction

Solid oxide fuel cells (SOFC) are of interest due to their ability to achieve high energy conversion efficiencies and their inherent fuel flexibility. Ni-YSZ composites (cermets) are the most commonly used anodes in SOFC due to the high electronic conductivity and catalytic activity of Ni, and their ease of fabrication. While Ni-YSZ cermet anodes have many positive attributes, they also have several limitations, including slow loss of surface area due to sintering of the Ni, low tolerance to hydrocarbon and sulfur impurities, and low redox stability.<sup>1–5</sup> Overcoming these limitations has recently motivated research into the development of anodes that use conductive ceramics to provide electronic conductivity. While a variety of conducting oxides, mostly in the perovskite family such as titanates,<sup>6–9</sup> manganates,<sup>10–13</sup> chromates<sup>14</sup> and bronzes<sup>15,16</sup> have been studied for use in SOFC anodes, in almost all cases these materials have relatively low catalytic activity for oxidation reactions resulting in high electrode overpotentials. Their performance improves significantly, however, upon the addition of nanoparticles of highly catalytic metals (e.g. Ni, Pt, or Pd) to the surface of the oxide.<sup>7,11,14–25</sup>

The catalytic metals are generally added using standard wet infiltration techniques. Recent work from the Barnett group, however, has shown that the catalytic metal nanoparticles can also be produced *in situ* via exsolution from an electronically conducting ceramic host.<sup>14,22–24,26</sup> This approach is similar to that used in so-called “intelligent” catalysts which were first

developed by researchers at Daihatsu for use in automotive emissions control systems.<sup>27–31</sup> One of the key insights in the Daihatsu work was the realization that while precious metals, such as Pd, were soluble on the B-site in perovskite oxides under oxidizing conditions, they had only limited solubility under reducing conditions. Thus, by changing between reducing and oxidizing conditions the metal could be substituted into and out of the perovskite lattice. This process is shown schematically in Fig. 1.

Barnett's initial studies of the use of this phenomena in SOFC anodes focused on the mixed conducting perovskite,  $\text{La}_{0.8}\text{Sr}_{0.2}\text{Cr}_{1-x}\text{Ru}_x\text{O}_{3-x}$ , and showed that upon reduction Ru nanoparticles <5 nm in diameter were formed *via* exsolution of Ru from the perovskite lattice.<sup>14,24</sup> Anodes composed of

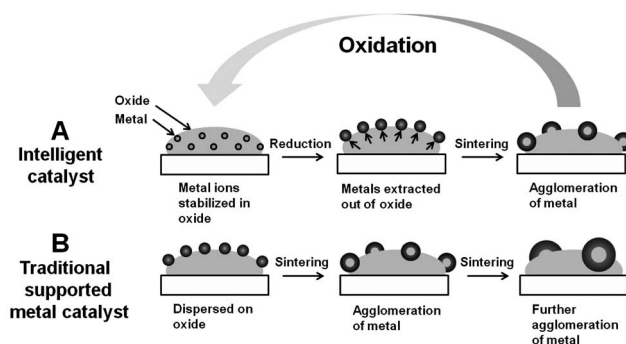


**Fig. 1** Panel A: schematic of an intelligent catalyst in which metals move out of and into an oxide host lattice in response to exposure to reducing and oxidizing conditions, respectively. Panel B: sintering of metal nanoparticles on an oxide which occurs over time for most traditional supported metal catalysts.

Department of Chemical and Biomolecular Engineering, University of Pennsylvania, 220 South 33rd Street 311A Towne Building, Philadelphia, Pennsylvania 19104-6315, USA. E-mail: adijanto@seas.upenn.edu; venu@seas.upenn.edu; kungas@seas.upenn.edu; gorte@seas.upenn.edu; vohs@seas.upenn.edu; Fax: +1 215-573-2093; Tel: +1 215-898-8351

composites of  $\text{La}_{0.8}\text{Sr}_{0.2}\text{Cr}_{1-x}\text{Ru}_x\text{O}_{3-x}$  and gadolinia-doped ceria (GDC) electrolyte were found to exhibit excellent performance after activation in  $\text{H}_2$ . They have subsequently expanded their studies to include the exsolution of Ni and Pd particles from electronically conducting (La, Sr) $\text{CrO}_3$ .<sup>22,26</sup>

The work from the Barnett group provides an exciting new paradigm for both optimizing the catalytic properties of ceramic anodes for SOFC for specific fuels and for maintaining long term performance. In order to obtain high performance anodes, this approach does require, however, the use of host oxides that have a high electronic conductivity. We and others have recently shown that alkaline earth (AE) doped rare earth (RE) vanadates ( $\text{RE}_{1-x}\text{AE}_x\text{VO}_4$ ), such as  $\text{Ce}_{1-x}\text{Sr}_x\text{VO}_4$  and  $\text{La}_{1-x}\text{Sr}_x\text{VO}_4$ , have electronic conductivities approaching  $1000 \text{ S cm}^{-1}$  under some conditions, and are chemically stable in a variety of fuels including  $\text{H}_2$ ,  $\text{H}_2\text{S}$ , and  $\text{CH}_4$ .<sup>32–39</sup> These materials have a zircon structure under oxidizing conditions but undergo a phase change to the perovskite structure upon reduction.<sup>32,40</sup> It is unclear, however, whether transition metals can be substituted into these materials, and whether they will undergo exsolution phenomena such as that described above. Thus, the goal of the work presented here was to investigate the suitability of transition metal substituted  $\text{RE}_{1-x}\text{AE}_x\text{VO}_4$  materials for use in SOFC anodes and to specifically determine whether the metal can be moved out of and into the lattice by redox cycling, and if this phenomenon can be used to tailor catalytic properties.

## Experimental

$\text{Ce}_{1-x}\text{TM}_x\text{VO}_{4-0.5x}$  materials (where TM = Ni, Co, Cu) were prepared using an aqueous precursor solution containing the appropriate amounts of  $\text{Ce}(\text{NO}_3)_3 \cdot 6\text{H}_2\text{O}$  (Alfa Aesar, 99.5%),  $\text{NH}_4\text{VO}_3$  (Aldrich, 99+%), and with either  $\text{Ni}(\text{NO}_3)_2 \cdot 6\text{H}_2\text{O}$ ,  $\text{Co}(\text{NO}_3)_2 \cdot 6\text{H}_2\text{O}$ , or  $\text{Cu}(\text{NO}_3)_2 \cdot 6\text{H}_2\text{O}$  (Alfa Aesar, 99.9%). Citric acid (Fisher Scientific) was also added as a complexing agent to aid in the formation of a single phase at a lower temperature. The precursor solution was then dried and the resulting powder was calcined at 973 K in air to form the zircon phase. Perovskite  $\text{Ce}_{1-x}\text{TM}_x\text{VO}_3$  materials were produced by reducing the  $\text{Ce}_{1-x}\text{TM}_x\text{VO}_{4-0.5x}$  in humidified  $\text{H}_2$  (3%  $\text{H}_2\text{O}$ ) at 973 K. Materials in which alkaline earth (AE) ions,  $\text{Sr}^{2+}$  and  $\text{Ca}^{2+}$ , were substituted for a portion of the cerium cations were also synthesized in a similar manner using  $\text{Sr}(\text{NO}_3)_2$  and  $\text{Ca}(\text{N-O}_3)_2 \cdot 4\text{H}_2\text{O}$  (Alfa Aesar, 99.9%) in the precursor solution.

Porous YSZ slabs into which 30 wt%  $\text{Ce}_{1-x}\text{TM}_x\text{VO}_{4-0.5x}$  or  $\text{Ce}_{1-y-x}\text{AE}_y\text{TM}_x\text{VO}_{4-0.5y-0.5x}$  (for simplicity we will refer to the latter compound as  $\text{Ce}_{1-x-y}\text{AE}_y\text{TM}_x\text{VO}_{4-\delta}$  throughout the remainder of the paper) had been infiltrated were used for hydrocarbon stability and conductivity measurements. The porous, 4 mm  $\times$  4 mm  $\times$  15 mm YSZ slabs were prepared using methods that have been described in detail previously.<sup>41,42</sup> The vanadates were added to the porous YSZ slabs by infiltrating the aqueous precursor solution followed by drying and annealing in air at 973 K. Multiple infiltration/annealing cycles were used to obtain the desired 30 wt% loading. For conductivity measurements, the  $\text{Ce}_{1-x-y}\text{AE}_y\text{TM}_x\text{VO}_{4-\delta}$ -YSZ composites were first pre-reduced at 973 K in humidified  $\text{H}_2$  (3%  $\text{H}_2\text{O}$ ) for 2 h. The conductivity was measured using the 4-probe, DC method with the sample in humidified  $\text{H}_2$  as a function of temperature.

The stability of the vanadates in hydrocarbons was assessed by exposing  $\text{Ce}_{1-x-y}\text{AE}_y\text{TM}_x\text{VO}_{4-\delta}$ -YSZ composites to dry methane at 973 K for 3 hours and measuring the weight gain resulting from carbon deposition. The morphological structure of the anode composites was determined using scanning electron microscopy (SEM) (FEI Quanta 600 ESEM) and X-ray diffraction (XRD) using  $\text{Cu K}_\alpha$  radiation. Powder samples were used for the XRD measurements and a small amount of YSZ was physically mixed with the vanadate powder to act as a reference. Surface areas of the composites were measured by the BET method using Kr adsorption at 78 K.

Cells 1 cm in diameter were used in all fuel cell measurements. These cells were fabricated using porous-dense-porous tri-layer YSZ wafers that were produced using tape casting methods that have been described in detail previously.<sup>41</sup> For each cell, the dense electrolyte layer was 80  $\mu\text{m}$  thick and 1 cm in diameter. The 60% porous YSZ layers on each side of the dense electrolyte layer were 50  $\mu\text{m}$  thick with a BET surface area  $0.3 \text{ m}^2 \text{ g}^{-1}$ . 40 wt% Sr-doped lanthanum ferrite,  $\text{La}_{0.8}\text{Sr}_{0.2}\text{FeO}_3$  (LSF), was added to one porous layer to form a cathode using multiple cycles of infiltration of an aqueous solution containing dissolved  $\text{La}(\text{N-O}_3)_3 \cdot 6\text{H}_2\text{O}$  (Alfa Aesar, 99.9%),  $\text{Sr}(\text{NO}_3)_2$  (Alfa Aesar, 99%) and  $\text{Fe}(\text{NO}_3)_3 \cdot 9\text{H}_2\text{O}$  (Fisher Scientific) in the appropriate molar ratios, followed by calcination in air at 723 K.<sup>43–45</sup> After the infiltration steps the composite cathode was calcined to 1123 K for 4 h to form the perovskite structure. The  $\text{Ce}_{1-x-y}\text{AE}_y\text{TM}_x\text{VO}_{4-\delta}$  anode was synthesized in a similar manner except that a 30 wt% loading was used and it was calcined to only 973 K and was reduced in humidified  $\text{H}_2$  (3%  $\text{H}_2\text{O}$ ) at 973 K prior to cell testing. Silver paste was applied to both electrodes and used as the current collector and the cells were mounted onto an alumina tube using a ceramic adhesive (Aremco, Ceramabond 552). All the cell tests were performed with the anode exposed to humidified  $\text{H}_2$  (3%  $\text{H}_2\text{O}$ ) and the cathode to ambient air. Electrochemical impedance spectra were measured between 0.1 Hz and 300 kHz with a 1 mA AC perturbation and  $V$ - $i$  polarization curves were measured using a Gamry Instruments potentiostat.

## Results and discussion

Initial studies focused on using XRD of the powder samples to determine the solubility limits of the transition metal dopants (Ni, Co, or Cu) within the zircon,  $\text{CeVO}_4$  structure. XRD allowed changes in the lattice parameter as a function of dopant concentration to be determined and the presence of secondary phases to be detected. Ni-doped  $\text{CeVO}_4$  will be used as an example to illustrate these methods. The zircon structure of  $\text{Ce}_{1-x}\text{Ni}_x\text{VO}_{4-0.5x}$  was confirmed by the presence of the expected diffraction peaks near 24.0, 32.4, 34.1, 36.4, 38.9, 43.2, 46.1, and 48.0 degrees  $2\theta$ .<sup>38,46</sup> Powder XRD patterns in the range 30 to 35 degrees  $2\theta$ , which contains the intense (112) peak of the zircon lattice between 32.39 and 32.42 degrees  $2\theta$  are shown in Fig. 2 for this material for several  $x$  values. Note that the peak at 30.1 degrees  $2\theta$  corresponds to the YSZ that was added as a standard.

In the bottom pattern in the figure, corresponding to  $\text{CeVO}_4$ , the (112) peak of the zircon lattice appears at 32.39 degrees  $2\theta$ . Substitution of 20 mol% of Ce cations with Ni cations ( $\text{Ce}_{0.8}\text{Ni}_{0.2}\text{VO}_{3.90}$ ) resulted in a shift of the (112) peak to 32.41 degrees  $2\theta$  due to a decrease in the lattice parameter. Assuming

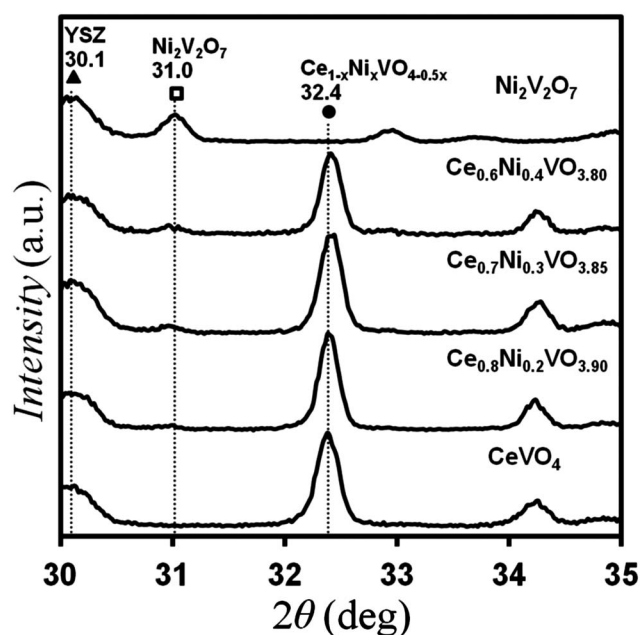


**Fig. 2** XRD patterns of  $\text{Ce}_{1-x}\text{Ni}_x\text{VO}_{4-0.5x}$ -YSZ composites that were calcined in air at 973 K for  $x$  values of 0, 0.2, 0.3, 0.4, 1. The peaks labeled ▲, □ and ● correspond to YSZ,  $\text{Ni}_2\text{V}_2\text{O}_7$  and  $\text{Ce}_{1-x}\text{Ni}_x\text{VO}_{4-0.5x}$ , respectively.

the formation of a single phase material with the zircon structure, Vegard's law<sup>46</sup> predicts that the lattice parameter (or the position of a characteristic diffraction peak) should be a linear function of the Ni concentration up to the solubility limit. At higher Ni concentrations the zircon lattice constant should remain fixed with secondary Ni-rich phases being formed. The plot of the position of the (112) diffraction peak as a function of  $x$  in  $\text{Ce}_{1-x}\text{Ni}_x\text{VO}_{4-0.5x}$  in Fig. 3 shows this characteristic behavior and indicates that the limiting value of  $x$  is 0.28. This result is consistent with the XRD data in Fig. 2 which show that for  $x$  values  $\geq 0.3$  an additional peak appears in the diffraction pattern at 31.0 degrees  $2\theta$  which can be assigned to  $\text{Ni}_2\text{V}_2\text{O}_7$  (for comparison purposes the XRD pattern of this compound is also included in the figure). The solubility limits for Co and Cu in  $\text{CeVO}_4$  were determined in an analogous manner and are reported in Table 1. Note that the solubility limits were nearly the same for all three metal cations,  $x \approx 0.28$ , which is consistent

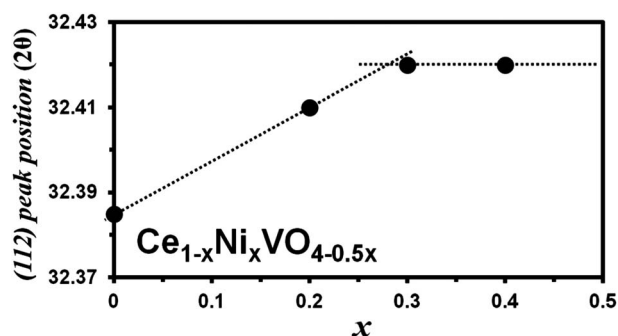


**Fig. 3** Plot of the position of the (112) diffraction peak as a function of  $x$  for  $\text{Ce}_{1-x}\text{Ni}_x\text{VO}_{4-0.5x}$ .

**Table 1** Transition metal solubility limit in  $\text{Ce}_{1-x}\text{TM}_x\text{VO}_{4-0.5x}$

Solid solubility limit			
$\text{Ce}_{1-x}\text{TM}_x\text{VO}_{4-0.5x}$	Ni	Co	Cu
$x$	0.28	0.25	0.28

with the fact that the ionic radii of these cations,  $\text{Ni}^{2+}$  (0.83 Å),  $\text{Co}^{2+}$  (0.79 Å),  $\text{Cu}^{2+}$  (0.87 Å), are similar.<sup>47</sup> In the remainder of the study in order to allow materials with similar compositions to be compared, a Ce : transition metal ratio of 0.8 : 0.2 was used.

To establish that the transition metal can reversibly move out of/into the oxide lattice in response to changes in the reducing/oxidizing atmospheres, a series of XRD measurements were performed for a  $\text{Ce}_{0.8}\text{Ni}_{0.2}\text{VO}_{3.90}$  sample that was exposed to both oxidizing (air) and reducing ( $\text{H}_2 + 3\% \text{H}_2\text{O}$ ) environments at 973 K for 2 h. Pattern A in Fig. 4 corresponds to the oxidized sample and contains peaks for the zircon lattice. As shown by pattern B in this figure, significant changes in the diffraction pattern occurred upon reduction of the sample in humidified  $\text{H}_2$ . As expected for reducing conditions, this diffraction pattern contains peaks indicative of a perovskite phase (labeled with ● symbols in the figure). The positions of the peaks for this phase are close to those reported previously for  $\text{CeVO}_3$ .<sup>32,40</sup> As shown in the inset in the figure, small peaks indicative of metallic Ni (44.5 degrees  $2\theta$ ) and  $\text{V}_2\text{O}_3$  (32.9 and 36.2 degrees  $2\theta$ ) are also present in the diffraction pattern for the reduced sample. These results therefore demonstrate that for cerium nickel vanadate the zircon to perovskite transition which occurs upon exposure to reducing conditions is accompanied by exsolution of at least a portion of the Ni from the lattice. Furthermore, pattern C in Fig. 4, which was obtained after annealing the reduced sample in air, only contains peaks characteristic of zircon  $\text{Ce}_{0.8}\text{Ni}_{0.2}\text{VO}_{3.90}$  and does not contain peaks indicative of Ni, NiO, or  $\text{Ni}_2\text{V}_2\text{O}_7$ ; thus, demonstrating that the exsolution of the transition metal is reversible upon re-oxidation.

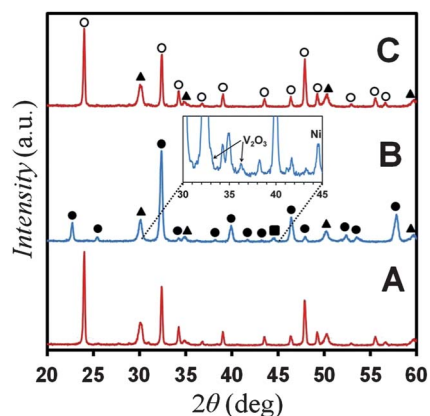


**Fig. 4** XRD patterns from a  $\text{Ce}_{0.8}\text{Ni}_{0.2}\text{VO}_{3.90}$  sample that was (A) oxidized at 973 K in air, (B) reduced at 973 K in humidified  $\text{H}_2$ , and (C) re-oxidized in air at 973 K. The peaks are labeled as follows: (▲) cubic YSZ, (○) zircon  $\text{Ce}_{0.8}\text{Ni}_{0.2}\text{VO}_{3.90}$ , (●) perovskite  $\text{Ce}_{1-x}\text{Ni}_x\text{VO}_3$ , and (■) metallic Ni.



The microstructure of the porous  $\text{Ce}_{0.8}\text{TM}_{0.2}\text{VO}_3$ -YSZ composite electrodes was investigated by SEM with resulting images shown in Fig. 5. Panel A in this figure is a micrograph of the porous YSZ prior to infiltration of the vanadate and shows that the YSZ matrix has a sponge-like appearance, with smooth pores ranging in size from 2 to 3  $\mu\text{m}$ . The micrograph in panel B was obtained after addition of 30 wt% of  $\text{Ce}_{0.8}\text{Ni}_{0.2}\text{VO}_{3.90}$ , followed by calcination in air at 973 K. The  $\text{Ce}_{0.8}\text{Ni}_{0.2}\text{VO}_{3.90}$  phase consists of what appears to be a relatively dense film composed of individual, interconnected  $\text{Ce}_{0.8}\text{Ni}_{0.2}\text{VO}_{3.90}$  particles that range in size from 10 to 20 nm. The BET surface area for the YSZ scaffold before infiltration of  $\text{Ce}_{0.8}\text{Ni}_{0.2}\text{VO}_{3.90}$  was 0.22  $\text{m}^2 \text{g}^{-1}$ . As shown in Table 2, which lists the BET surface area of the  $\text{Ce}_{0.8}\text{Ni}_{0.2}\text{VO}_{3.90}$ -YSZ composite as a function of oxidation and reduction treatments, the surface area of the freshly prepared  $\text{Ce}_{0.8}\text{Ni}_{0.2}\text{VO}_{3.90}$ -YSZ composite (redox cycle 1) was 0.30  $\text{m}^2 \text{g}^{-1}$ . The similarity in surface areas of the bare YSZ scaffold (0.22  $\text{m}^2 \text{g}^{-1}$ ) and the composite is consistent with the infiltrated  $\text{Ce}_{0.8}\text{Ni}_{0.2}\text{VO}_{3.90}$  film being relatively dense.

The SEM image of the  $\text{Ce}_{0.8}\text{Ni}_{0.2}\text{VO}_{3.90}$ -YSZ composite obtained after reduction in humidified  $\text{H}_2$  at 973 K (panel C, Fig. 5) was similar to that of the oxidized sample and no significant changes in the microstructure of the vanadate film are readily apparent. In particular, the SEM image does not provide any evidence for the formation of Ni particles; however, as shown in Table 2, reduction did result in a more than three-fold increase in the BET surface area from 0.30 to 1.07  $\text{m}^2 \text{g}^{-1}$ . This result suggests that the Ni that is exsolved during the transition of the vanadate from the zircon to the perovskite phase must be in the form of high surface area nanoparticles that are too small to be resolved in the SEM image.

To further confirm that the transition metal is being exsolved from the lattice under reducing conditions,  $\text{Ce}_{0.8}\text{TM}_{0.2}\text{VO}_3$ -YSZ composite samples were exposed to dry methane at 973 K for 3 h. Since most transition metals, including Ni and Co, are known to catalyze the formation of carbon filaments (*i.e.* multi-walled

**Table 2** BET surface areas of  $\text{Ce}_{0.8}\text{Ni}_{0.2}\text{VO}_{3.90}$ -YSZ composites

Redox cycle		Surface area ( $\text{m}^2 \text{g}^{-1}$ )
1	Oxidized	0.30
	Reduced	1.07
2	Oxidized	0.31
	Reduced	1.11

carbon nanotubes), this treatment would be expected to produce such filaments if metal nanoparticles are present on the surface of the vanadate. SEM images obtained after this treatment for  $\text{CeVO}_3$ ,  $\text{Ce}_{0.8}\text{Ni}_{0.2}\text{VO}_3$ ,  $\text{Ce}_{0.8}\text{Co}_{0.2}\text{VO}_3$ , and  $\text{Ce}_{0.8}\text{Cu}_{0.2}\text{VO}_3$  are displayed in Fig. 6 and the % weight gain for each sample is listed in Table 3. Panel A in Fig. 6 corresponds to the  $\text{CH}_4$ -treated  $\text{CeVO}_3$ -YSZ composite. This image is essentially identical to that obtained prior to  $\text{CH}_4$  exposure and does not contain any evidence for carbon deposition. This conclusion is supported by the fact that the weight of this sample changed by less than 1% after  $\text{CH}_4$  exposure.

A significantly different result was obtained for the  $\text{Ce}_{0.8}\text{Ni}_{0.2}\text{VO}_3$ -YSZ (panel B, Fig. 6) and  $\text{Ce}_{0.8}\text{Co}_{0.2}\text{VO}_3$ -YSZ (panel C, Fig. 6) composites. For these samples, worm-like features corresponding to carbon filaments are clearly evident in the micrographs. The weight gains for the  $\text{Ce}_{0.8}\text{Ni}_{0.2}\text{VO}_3$  and  $\text{Ce}_{0.8}\text{Co}_{0.2}\text{VO}_3$  samples were also 27 and 10%, respectively, further confirming that carbon deposition has occurred. These results clearly demonstrate the presence of Ni and Co nanoparticles on the surface of these reduced samples. For  $\text{Ce}_{0.8}\text{Cu}_{0.2}\text{VO}_3$  (panel D, Fig. 6), carbon filament formation was not observed, nor was there any weight gain following exposure to  $\text{CH}_4$ . As has previously been shown,<sup>17,48,49</sup> Cu is relatively non-catalytic and does not promote carbon filament growth for the conditions used in these experiments; thus, it is likely that Cu nanoparticles were also formed upon reduction of this material.

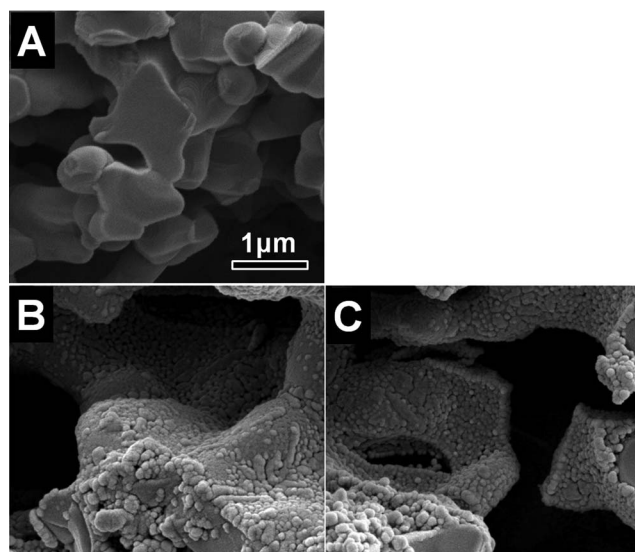


**Fig. 5** SEM images of (A) the bare YSZ matrix, and the  $\text{Ce}_{0.8}\text{Ni}_{0.2}\text{VO}_{3.90}$ -YSZ composite (B) oxidized in air at 973 K, and (C) reduced in humidified  $\text{H}_2$  at 973 K.

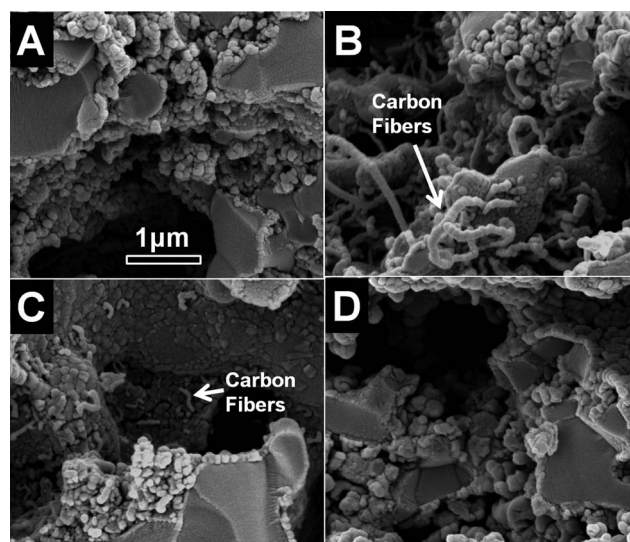


**Fig. 6** SEM images of the (A)  $\text{CeVO}_3$ -YSZ, (B)  $\text{Ce}_{0.8}\text{Ni}_{0.2}\text{VO}_3$ -YSZ, (C)  $\text{Ce}_{0.8}\text{Co}_{0.2}\text{VO}_3$ -YSZ, (D)  $\text{Ce}_{0.8}\text{Cu}_{0.2}\text{VO}_3$ -YSZ composites that had been exposed to dry methane at 973 K for 3 h.

**Table 3** The percentage weight changes measured after reducing the samples in humidified  $H_2$  at 973 K for 2 h before exposing them to dry methane at 973 K for 3 h

Sample	% Weight gain after exposure to dry $CH_4$ at 973 K
$Ce_{0.8}Ni_{0.2}VO_3$	27
$Ce_{0.8}Co_{0.2}VO_3$	10
$Ce_{0.8}Cu_{0.2}VO_3$	<1
$CeVO_3$	<1
$Ce_{0.7}Sr_{0.3}VO_3$	<1

To investigate the electrochemical performance of the transition-metal doped  $CeVO_3$  in SOFC anodes, button cells were prepared with an 80  $\mu m$  thick YSZ electrolyte, an infiltrated 30 wt%  $Ce_{0.8}TM_{0.2}VO_{3.85}$ -YSZ composite anode, and a 40 wt% LSF-YSZ composite cathode. For comparison purposes, cells with an infiltrated  $CeVO_3$  anode were also fabricated. For one of these cell the catalytic activity of the anode was enhanced by the addition of 1 wt% Pd by infiltration with aqueous solution of  $(NH_3)_4Pd(NO_3)_2$ . In order to produce the conductive phase of the vanadate, the anodes were initially reduced in humidified  $H_2$  at 973 K.  $V$ - $i$  polarization curves and impedance spectra for these cells operated at 973 K in humidified  $H_2$  are shown in Fig. 7, with the electrochemical performances summarized in Table 4.

The  $V$ - $i$  polarization (Fig. 7a) curves show that the cells each had an open-circuit potential near the theoretical Nernst value of 1.1 V. The Nyquist plots of the impedance spectra collected at open circuit (Fig. 7b) also show that the ohmic loss for each cell, calculated from the high-frequency intercept with the real axis, was  $\sim 0.4 \Omega cm^2$ , which is close to the expected value for the

**Table 4** Maximum power density and anode ASR

Anode material	Maximum power density ( $W cm^{-2}$ )	Anode ASR ( $\Omega cm^2$ )
$Ce_{0.8}Ni_{0.2}VO_3$	0.31	0.8
$Ce_{0.8}Co_{0.2}VO_3$	0.30	0.9
$Ce_{0.8}Cu_{0.2}VO_3$	0.14	1.4
$CeVO_3$	0.07	2.7
$Ce_{0.7}Sr_{0.1}Ni_{0.2}VO_3$	0.31	0.8

80  $\mu m$  thick YSZ electrolyte layer. This demonstrates that the vanadates provide adequate conductivity for the 50  $\mu m$  thick anodes used here. As will be discussed below, enhancements in electronic conductivity may be needed, however, if thicker electrodes are used. Since LSF-YSZ cathodes identical to those used here have previously been shown to have an ASR of  $\sim 0.2 \Omega cm^2$ ,<sup>43,44</sup> the anode ASR can be obtained by subtracting from the total resistance the ohmic ( $0.4 \Omega cm^2$ ) and cathode ( $0.2 \Omega cm^2$ ) contributions.

Note the relatively poor electrochemical performance obtained from the cells with the  $CeVO_3$ -YSZ and  $Ce_{0.8}Cu_{0.2}VO_3$ -YSZ composite anodes which had maximum current densities (Table 4) of only 0.07 and 0.14  $W cm^{-2}$  and anode area specific resistances (ASR) of 2.7 and 1.4  $\Omega cm^2$ , respectively. This poor performance is indicative of the low catalytic activity of both  $CeVO_3$  and Cu. Much better performance was obtained for the cells with  $Ce_{0.8}Ni_{0.2}VO_3$ -YSZ and  $Ce_{0.8}Co_{0.2}VO_3$ -YSZ composite anodes. These cells both had maximum power densities of 0.30  $W cm^{-2}$  and anode ASR of 0.9  $\Omega cm^2$ . This result is consistent with the presence of Ni or Co nanoparticles on the surface of the anode, both of which have high catalytic activity for  $H_2$  oxidation. It is noteworthy that nearly the same maximum power density was obtained from a cell with a  $CeVO_3$ -YSZ anode to which 1 wt% Pd had been added.

While the cell performance and impedance data indicate that for the relatively thin anodes used in this study the  $Ce_{0.8}TM_{0.2}VO_3$ -YSZ composites have adequate electronic conductivity, our previous studies of  $CeVO_3$ -YSZ composites<sup>39</sup> suggest that this may not be the case if thicker anodes, such as those in an anode supported cell, are used. In this previous work we showed that  $CeVO_3$ -YSZ composites with a structure similar to those used in the present study had an electronic conductivity of only 0.1  $S cm^{-1}$  at 973 K. It was found, however, that doping the cerium vanadate with +2 alkaline earth which had much higher electronic conductivity.<sup>39</sup> For example, the conductivity of a  $Ce_{0.7}Sr_{0.3}VO_3$ -YSZ composite was 9  $S cm^{-1}$  at 973 K. In order to determine if this method of enhancing the electronic conductivity would also work for the transition metal substituted cerium vanadates, we investigated the effect of substituting  $Sr^{2+}$  and  $Ca^{2+}$  for a portion of the  $Ce^{3+}$  in  $Ce_{0.8}Ni_{0.2}VO_3$ .

XRD analysis indicated that upon reduction the Ca- and Sr-substituted vanadates also formed the perovskite phase. The electrical conductivities of reduced  $Ce_{0.7}AE_{0.1}Ni_{0.2}VO_3$ -YSZ composites in humidified  $H_2$  are reported in Fig. 8 as a function of temperature. For comparison purposes, data for vanadates without Ni substitution are also included in the figure.

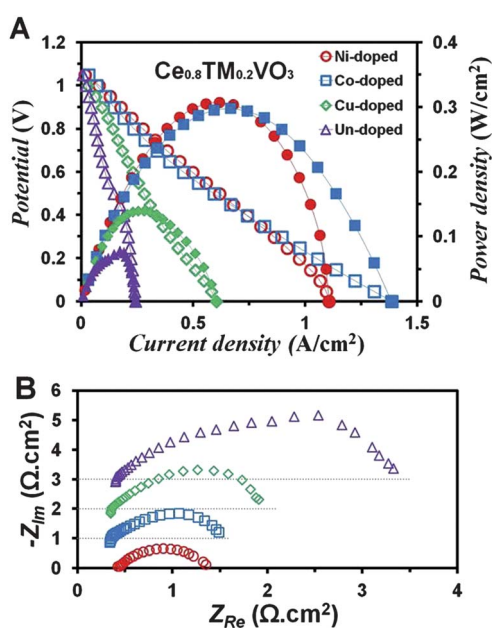


**Fig. 7** (A)  $V$ - $i$  polarization curves and (B) electrochemical impedance spectra of cells with infiltrated 30 wt% of (●)  $Ce_{0.8}Ni_{0.2}VO_3$ -YSZ, (■)  $Ce_{0.8}Co_{0.2}VO_3$ -YSZ, (◆)  $Ce_{0.8}Cu_{0.2}VO_3$ -YSZ, and (▲)  $CeVO_3$ -YSZ anodes. The cells were operated at 973 K with humidified  $H_2$  fuel.

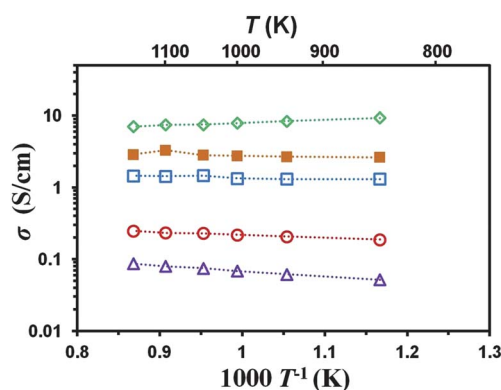


**Fig. 8** Electronic conductivities of infiltrated 30 wt% (Δ) CeVO<sub>3</sub>-YSZ, (○) Ce<sub>0.8</sub>Ni<sub>0.2</sub>VO<sub>3</sub>-YSZ, (□) Ce<sub>0.7</sub>Sr<sub>0.1</sub>Ni<sub>0.2</sub>VO<sub>3</sub>-YSZ, (■) Ce<sub>0.7</sub>Ca<sub>0.1</sub>Ni<sub>0.2</sub>VO<sub>3</sub>-YSZ, (◇) Ce<sub>0.7</sub>Sr<sub>0.3</sub>VO<sub>3</sub>-YSZ composites in humidified H<sub>2</sub> as a function of temperature.

The samples used in this series of experiments consisted of porous slabs of YSZ (60% porosity) into which 30 wt% of the vanadate was infiltrated using the method described in the experimental section. The use of composites manufactured in this way simplified sample preparation compared to that for bulk samples since high-temperature sintering was not required to produce dense bodies. The porous composites also had structures that closely approximate those used in actual electrochemical devices, such as a SOFC, allowing the conductivity values to be used to predict the properties of real electrodes. Note that the conductivities of the bulk materials would be expected to be at least an order of magnitude higher than those of the composites.<sup>35,50,51</sup> In each case, the samples were held at the measurement temperature for 30 minutes to equilibrate. As expected, the alkaline earth doped Ce<sub>0.7</sub>(Sr/Ca)<sub>0.1</sub>Ni<sub>0.2</sub>VO<sub>3</sub>-YSZ composites all exhibited conductivities that were at least an order of magnitude higher than those for the non-calcium or strontium containing analogs. The conductivities at 973 K for the Ce<sub>0.7</sub>Sr<sub>0.1</sub>Ni<sub>0.2</sub>VO<sub>3</sub>-YSZ the Ce<sub>0.7</sub>Ca<sub>0.1</sub>Ni<sub>0.2</sub>VO<sub>3</sub>-YSZ composites were 2 and 3.0 S cm<sup>-1</sup>, respectively.

One potential advantage of using transition-metal doped cerium vanadate in SOFC anodes is that these materials may exhibit high redox stability, since the metal reversibly moves in and out of the lattice upon exposure to oxidizing and reducing conditions. In order to test this possibility, a fuel cell with a Ce<sub>0.7</sub>Sr<sub>0.1</sub>Ni<sub>0.2</sub>VO<sub>3</sub>-YSZ anode was tested and subjected to redox cycling. This cell had a maximum power density of 0.31 W cm<sup>-2</sup> at 0.5 V while operating on humidified H<sub>2</sub> at 973 K. Fig. 9 displays the maximum power density of this cell as a function of time on stream. During the first hour of operation some degradation in performance is evident with the maximum current density decreasing to 0.26 W cm<sup>-2</sup>. This degradation may be due at least in part to sintering of the exsolved metal nanoparticles. The cell was then subjected to an oxidation treatment which consisted of exposing the anode to air for 30 min followed by reduction in humidified H<sub>2</sub> for 15 min, both at 973 K. As shown in the figure, this oxidation treatment had no adverse affect on the cell performance with the maximum current density increasing to 0.33 W cm<sup>-2</sup>. The cell performance was also found to remain relatively stable after several additional redox cycles.

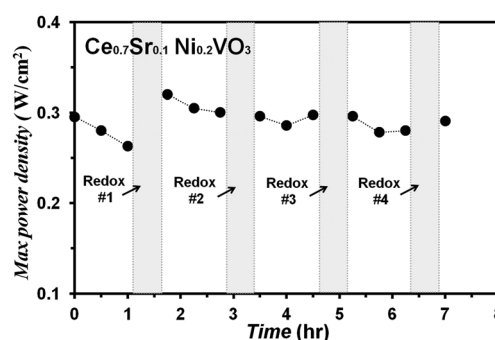


**Fig. 9** Maximum power density for a cell with an infiltrated 30 wt% of Ce<sub>0.7</sub>Sr<sub>0.1</sub>Ni<sub>0.2</sub>VO<sub>3</sub>-YSZ anode as a function of time at 973 K with humidified H<sub>2</sub> fuel. The cell was periodically subjected to a redox treatment consisting of oxidation in air for 30 min followed by reduction in humidified H<sub>2</sub> for 15 min, both at 973 K.

## Summary and conclusions

In this study it was demonstrated that upon reduction in humidified hydrogen at 973 K zircon-type Ce<sub>1-x</sub>TM<sub>x</sub>VO<sub>4-0.5x</sub> oxides undergo a phase transition to the perovskite structure which is accompanied by exsolution of a portion of the transition metal from the lattice. The exsolved metal forms nanoparticles that decorate the surface of the oxide. Furthermore, this process was demonstrated to be reversible with the metal moving back into the oxide lattice upon exposure to an oxidizing environment at 973 K, resulting in reformation of zircon Ce<sub>1-x</sub>TM<sub>x</sub>VO<sub>4-0.5x</sub>. The movement of the transition metal into and out of the lattice upon redox cycling is analogous to previously described intelligent perovskite-based catalysts.<sup>14,22-24,26-31</sup>

The metal exsolution process coupled with the high electronic conductivity of the alkaline earth-doped cerium vanadates makes them particularly attractive for use in SOFC anodes. The electronic conductivity of Ce<sub>0.7</sub>Sr<sub>0.1</sub>Ni<sub>0.2</sub>VO<sub>3</sub>-YSZ anodes that were synthesized using wet infiltration were found to be in excess of 1 S cm<sup>-1</sup> at 973 K under reducing conditions. The exsolved Ni nanoparticles exhibited high catalytic activity for H<sub>2</sub> oxidation and a cell with an anode of this design with an 80 μm thick YSZ electrolyte and LSF-YSZ composite anode exhibited a maximum power density of 0.31 W cm<sup>-2</sup> at 973 K. More importantly, the anode in this cell had unusually high redox stability with exposure to air at 973 K not resulting in any performance degradation or mechanical instabilities. These properties suggest that one may be able to use redox cycling to regenerate any activity loss exhibited by these anodes over time. For example, sintering of the catalytic metal nanoparticles causing loss of reactive surface area and performance degradation could be reversed by an oxidation/reduction cycle in which the metal is re-dissolved into the vanadate during the oxidation treatment, followed by metal nanoparticles being reformed when the anode is exposed to the H<sub>2</sub>-rich reactant stream (shown schematically in Fig. 1).

It should be noted that while most of the anodes studied in the present investigation were not hydrocarbon tolerant due to the fact that both Co and Ni catalyze the formation of carbon filaments when exposed to hydrocarbons under reducing conditions, the results of this study do suggest a strategy for using the cerium



vanadate-based materials to produce hydrocarbon tolerant electrodes. As we have reported previously, SOFC anodes that use Cu-rich, Ni–Cu alloys for both the catalyst and electronically conductive component exhibit high activity and relatively high hydrocarbon tolerance.<sup>3,52,53</sup> Even higher hydrocarbon tolerance has been obtained for anodes using mixtures of Cu and Co where stable performance while operating on dry methane at 1073 K has been reported.<sup>53–56</sup> In this latter case the two metals do not form an alloy, but rather due to copper's low surface free energy, the surface of the metal particles in the anode is enriched in the relatively un-reactive Cu, although enough Co atoms remain exposed to maintain high catalytic activity.<sup>53–56</sup> Since in the present investigation we have demonstrated that Cu, Ni, and Co can be substituted into the alkaline earth doped cerium vanadates, it may be possible to synthesize vanadates that contain a mixture of Cu and Co or Cu and Ni. For these materials exsolution of the metals under reducing conditions may produce catalyst particles with high hydrocarbon tolerance. This strategy is currently under investigation.

## Acknowledgements

We thank the US Office of Naval Research for support (grant no. N00014-11-1-0229) for this work.

## References

- M. L. Toebes, J. H. Bitter, A. J. van Dillen and K. P. de Jong, *Catal. Today*, 2002, **76**, 33–42.
- C. H. Toh, P. R. Munroe, D. J. Young and K. Foger, *Mater. High Temp.*, 2003, **20**, 129–136.
- H. Kim, C. Lu, W. L. Worrell, J. M. Vohs and R. J. Gorte, *J. Electrochem. Soc.*, 2002, **149**, A247–A250.
- Y. Matsuzaki and I. Yasuda, *Solid State Ionics*, 2000, **132**, 261–269.
- D. Sarantaridis and A. Atkinson, *Fuel Cells*, 2007, **7**, 246–258.
- M. D. Gross, K. M. Carver, M. A. Deighan, A. Schenkel, B. M. Smith and A. Z. Yee, *J. Electrochem. Soc.*, 2009, **156**, B540–B545.
- S. Lee, G. Kim, J. M. Vohs and R. J. Gorte, *J. Electrochem. Soc.*, 2008, **155**, B1179–B1183.
- D. Neagu and J. T. S. Irvine, *Chem. Mater.*, 2010, **22**, 5042–5053.
- A. Vincent, J. L. Luo, K. T. Chuang and A. R. Sanger, *J. Power Sources*, 2010, **195**, 769–774.
- G. Kim, G. Corre, J. T. S. Irvine, J. M. Vohs and R. J. Gorte, *Electrochem. Solid-State Lett.*, 2008, **11**, B16–B19.
- G. Kim, S. Lee, J. Y. Shin, G. Corre, J. T. S. Irvine, J. M. Vohs and R. J. Gorte, *Electrochem. Solid-State Lett.*, 2009, **12**, B48–B52.
- S. W. Tao and J. T. S. Irvine, *Nat. Mater.*, 2003, **2**, 320–323.
- M. van den Bossche, R. Matthews, A. Lichtenberger and S. McIntosh, *J. Electrochem. Soc.*, 2010, **157**, B392–B399.
- W. Kobsiriphat, B. D. Madsen, Y. Wang, L. D. Marks and S. A. Barnett, *Solid State Ionics*, 2009, **180**, 257–264.
- L. Adjianto, R. Kungas, J. Park, J. M. Vohs and R. J. Gorte, *Int. J. Hydrogen Energy*, 2011, **36**, 15722–15730.
- B. H. Smith and M. D. Gross, *Electrochem. Solid-State Lett.*, 2011, **14**, B1–B5.
- R. J. Gorte, S. Park, J. M. Vohs and C. H. Wang, *Adv. Mater.*, 2000, **12**, 1465–1469.
- M. D. Gross, J. M. Vohs and R. J. Gorte, *J. Electrochem. Soc.*, 2007, **154**, B694–B699.
- J. S. Kim, V. V. Nair, J. M. Vohs and R. J. Gorte, *Scr. Mater.*, 2011, **65**, 90–95.
- Z. H. Bi and J. H. Zhu, *J. Electrochem. Soc.*, 2011, **158**, B605–B613.
- A. Babaei, L. Zhang, S. L. Tan and S. P. Jiang, *Solid State Ionics*, 2010, **181**, 1221–1228.
- D. M. Bierschenk, E. Potter-Nelson, C. Hoel, Y. G. Liao, L. Marks, K. R. Poeppelmeier and S. A. Barnett, *J. Power Sources*, 2011, **196**, 3089–3094.
- B. D. Madsen, W. Kobsiriphat, Y. Wang, L. D. Marks and S. A. Barnett, *J. Power Sources*, 2007, **166**, 64–67.
- Y. Wang, B. D. Madsen, W. Kobsiriphat, S. A. Barnett and L. D. Marks, *Microsc. Microanal.*, 2007, **13**, 100–101.
- G. L. Xiao, C. Jin, Q. Liu, A. Heyden and F. L. Chen, *J. Power Sources*, 2012, **201**, 43–48.
- W. Kobsiriphat, B. D. Madsen, Y. Wang, M. Shah, L. D. Marks and S. A. Barnett, *J. Electrochem. Soc.*, 2010, **157**, B279–B284.
- Y. Nishihata, J. Mizuki, T. Akao, H. Tanaka, M. Uenishi, M. Kimura, T. Okamoto and N. Hamada, *Nature*, 2002, **418**, 164–167.
- I. Tan, M. Taniguchi, H. Tanaka, M. Uenishi, N. Kajita, Y. Nishihata, J. Mizuki and K. Niihara, *Science of Engineering Ceramics III, Key Engineering Materials*, 2006, **317–318**, 833–836.
- H. Tanaka, M. Taniguchi, M. Uenishi, N. Kajita, I. Tan, Y. Nishihata, J. Mizuki, K. Narita, M. Kimura and K. Kaneko, *Angew. Chem., Int. Ed.*, 2006, **45**, 5998–6002.
- H. Tanaka, M. Uenishi, M. Taniguchi, I. Tan, K. Narita, M. Kimura, K. Kaneko, Y. Nishihata and J. Mizuki, *Catal. Today*, 2006, **117**, 321–328.
- M. Taniguchi, H. Tanaka, M. Uenishi, I. Tan, Y. Nishihata, J. Mizuki, H. Suzuki, K. Narita, A. Hirai and M. Kimura, *Top. Catal.*, 2007, **42–43**, 367–371.
- N. Danilovic, J. L. Luo, K. T. Chuang and A. R. Sanger, *J. Power Sources*, 2009, **192**, 247–257.
- M. Cooper, K. Channa, R. De Silva and D. J. Bayless, *J. Electrochem. Soc.*, 2010, **157**, B1713–B1718.
- C. Peng, J. L. Luo, A. R. Sanger and K. T. Chuang, *Chem. Mater.*, 2010, **22**, 1032–1037.
- J. S. Park, I. D. Hasson, M. D. Gross, C. Chen, J. M. Vohs and R. J. Gorte, *J. Power Sources*, 2011, **196**, 7488–7494.
- Z. Cheng, S. W. Zha, L. Aguilar and M. L. Liu, *Solid State Ionics*, 2005, **176**, 1921–1928.
- C. T. G. Petit, R. Lan, P. I. Cowin, A. Kraft and S. W. Tao, *J. Mater. Sci.*, 2011, **46**, 316–326.
- C. T. G. Petit, R. Lan, P. I. Cowin, J. T. S. Irvine and S. W. Tao, *J. Mater. Chem.*, 2011, **21**, 525–531.
- L. Adjianto, V. Balaji Padmanabhan, K. J. Holmes, R. J. Gorte and J. M. Vohs, *J. Solid State Chem.*, 2012, DOI: 10.1016/j.jssc.2012.01.065.
- E. V. Tsipis, V. V. Kharton, N. P. Vyshatko, A. L. Shaula and J. R. Frade, *J. Solid State Chem.*, 2003, **176**, 47–56.
- S. Park, R. J. Gorte and J. M. Vohs, *J. Electrochem. Soc.*, 2001, **148**, A443–A447.
- R. Kungas, J. S. Kim, J. M. Vohs and R. J. Gorte, *J. Am. Ceram. Soc.*, 2011, **94**, 2220–2224.
- W. S. Wang, M. D. Gross, J. M. Vohs and R. J. Gorte, *J. Electrochem. Soc.*, 2007, **154**, B439–B445.
- J. M. Vohs, L. Adjianto, R. Kungas, F. Bidrawn and R. J. Gorte, *J. Power Sources*, 2011, **196**, 5797–5802.
- R. J. Gorte and J. M. Vohs, *Adv. Mater.*, 2009, **21**, 943–956.
- A. Watanabe, *J. Solid State Chem.*, 2000, **153**, 174–179.
- R. S. Devan, Y. D. Kolekar and B. K. Chougule, *J. Phys.: Condens. Matter*, 2006, **18**, 9809–9821.
- S. McIntosh and R. J. Gorte, *Chem. Rev.*, 2004, **104**, 4845–4865.
- R. J. Gorte, J. M. Vohs and S. McIntosh, *Solid State Ionics*, 2004, **175**, 1–6.
- X. H. Fang, G. Y. Zhu, C. R. Xia, X. Q. Liu and G. Y. Meng, *Solid State Ionics*, 2004, **168**, 31–36.
- W. Z. Zhu and S. C. Deevi, *Mater. Sci. Eng., A*, 2003, **362**, 228–239.
- S. Jung, M. D. Gross, R. J. Gorte and J. M. Vohs, *J. Electrochem. Soc.*, 2006, **153**, A1539–A1543.
- S. I. Lee, J. M. Vohs and R. J. Gorte, *J. Electrochem. Soc.*, 2004, **151**, A1319–A1323.
- S. I. Lee, K. Ahn, J. M. Vohs and R. J. Gorte, *Electrochem. Solid-State Lett.*, 2005, **8**, A48–A51.
- S. W. Jung, J. M. Vohs and R. J. Gorte, *J. Electrochem. Soc.*, 2007, **154**, B1270–B1275.
- M. D. Gross, J. M. Vohs and R. J. Gorte, *Electrochim. Acta*, 2007, **52**, 1951–1957.